Article

Superparamagnetic Iron Oxide Nanoparticle Nanodevices Based on Fe₃O₄ Coated by Megluminic Ligands for the Adsorption of Metal Anions from Water

Stefano Scurti, Sandro Dattilo,* David Gintsburg, Luigi Vigliotti, Aldo Winkler, Sabrina Carola Carroccio, and Daniele Caretti

Read Online

ACCESS | Metrics & More | Article Recommendations | Supporting Information

ABSTRACT: The uptake ability toward arsenic(V), chromium(VI), and boron(III) ions of ad hoc functionalized magnetic nanostructured devices has been investigated. To this purpose, ligands based on meglumine have been synthesized and used to coat magnetite nanoparticles (Fe₃O₄) obtained by the co-precipitation methodology. The as-prepared hybrid material was characterized by infrared spectroscopy (IR), X-ray diffraction, thermogravimetric analysis, and scanning electron microscopy combined with energy-dispersive X-ray analysis. Moreover, its magnetic hysteresis properties were measured to evaluate its magnetic properties, and the adsorption kinetics and isothermal models were applied to discern between the different adsorption phenomena. Specifically, the better fitting was observed by the Langmuir isotherm model for all metal ions tested, highlighting a higher uptake in arsenic (28.2 mg/g), chromium (12.3 mg/g), and boron (23.7 mg/g) sorption values if compared with other magnetic nanostructured materials. After adsorption, an external magnetic stimulus can be used to efficiently remove nanomaterials from the water. Finally the nanomaterial can be reused up to five cycles and regenerated for another three cycles.
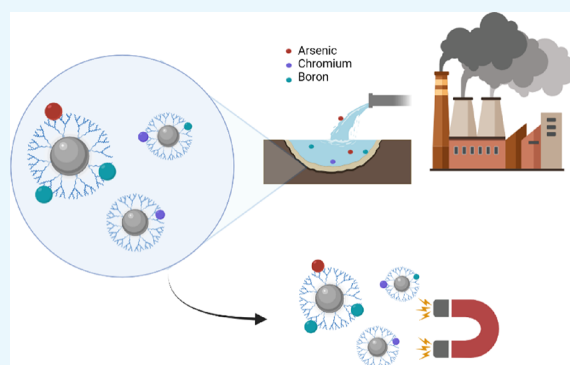
1. INTRODUCTION

In light of the increasing issues related to exhausted water resources, global warming, and environmental pollution, in the last years, water decontamination represents one of the main goals to be achieved. In this scenario, the water control intended for human consumption derived from underground aquifers or surface reservoirs represents an achievement of crucial importance. Indeed, the prolonged contact of water with the surroundings causes the dissolution or the float of compounds derived from the earth background or anthropogenic activities.[1−4] In particular, harmful and toxic metal ions present in water have become a global critical issue, and the severe environmental pollution represents a danger to human health and aquatic life.[5] Moreover, the non-biodegradability of these pollutants ensures the tendency to accumulate in living organisms.[6,7] Generally, metal ions are not removed even after the wastewater treatments by sewage treatment plants, increasing the risk of soil contamination and subsequently of the food chain.[8−10] Intake of them by the food chain has been widely reported, and as a consequence, several pathologies have been observed deriving from pollutant bioaccumulation.[11−14]

To protect the aquatic and the human life, it is now urgent to develop industrially scalable and easy applicable strategies in existing plants to treat contaminated water prior to its discharge into the environment. Various chemical and physical processes have been used for wastewater treatment in order to reduce the pollutant amount values under the law limit.[15−19] Although most of the existing metal anion removal technologies have exhibited high efficiency in the lab scale, several issues are arisen due to their high cost, complex procedures, and pretreatment processes. Among various techniques for removing toxic metal ions from wastewater, adsorption is found to be one of the most effective and feasible due to the simplicity of the design, initial cost, and to reduce operation and insensitivity to harmful pollutants.[20,21] Additionally, adsorbing materials are able to guarantee flexibility in design and operation but are also characterized by reversibility in order to regenerate them for multiple use through a suitable desorption method bearing to the low maintenance cost.[22−24] In this optic, meglumine (MEG)-functionalized materials have represented a solution for the metal ion uptake due to its high

efficiency and selectivity toward metal ions such us chromium, arsenic, and boron.[25−27] First, this ligand is used for a selective boron removal from the water constituting the chelating moiety of different ion-exchange commercial products based on polymeric resins.[27−32]

However, it was demonstrated that it also exhibited excellent sorption capability for other metal anions such as arsenic, chromium, antimuonium, and germanium, although in the presence of antagonist anions.[25,27,29] Regarding this topic, the employ of high-gradient magnetic separation-based technologies combined with the adsorption approach by the use of magnetic stimuli-responsive materials represents an efficient strategy to water treatment.[21,33−37] Moreover, in the recent years, proof of concept as well as prototype technologies, showed that magnetic nanosized metal oxide can be proficiently used for environmental purposes.[31,38−42] Indeed, by the application of external magnetic stimulus, the devices can be easily removed from the water, refreshed, and reused. Especially, the application of superparamagnetic iron oxide nanoparticles (SPIONs) has been extensively studied to prepare a functional magnetic nanosorbent.[43,44] Recent works have proposed a series of the functionalized nanostructured materials in order to enhance the adsorption capacity and/or selectivity against specific pollutants by tuning their surface chemistry and physical properties. Alam et al. have prepared $Fe_3O_4@mSiO_2-NH_2$ magnetic core−shell amino adsorbents by a multistep sol−gel methodology able to uptake heavy metal cations such as Zn, Pb, and Cu, where the magnetic element was used similar to a support and the adsorbent phase was bonded onto a metal surface by click chemistry.[45]

Another approach is the direct use of SPIONs similar to adsorbent materials before their deposition onto the support, and Das's group have employed nanomagnetic particles to decorate graphene oxide (GO) in order to obtain high-efficient iron-graphene oxide nanohybrid materials in terms of adsorption capability against As(III) and As(V).[46] The same strategy has been used by Yuan et al. to immobilize SPIONs onto montmorillonite to enhance the Cr(VI) adsorption with respect to unsupported nanoparticles.[47] In addition, magnetic nanocomposites with a range of organic coatings were prepared by Guivar and co-workers in order to investigate the correlation between the ligands and surface properties, as well as the adsorption capability against copper and lead.[48] A strict dependence between the ligand chemistry and the material uptake properties has been observed, and this opens the possibility to tune the SPION features with specific functionalized ligands in order to improve their adsorption efficiency and selectivity.

In this view, we have exploited the synergistic effects of both high surface area and magnetic properties of SPIONs and the huge affinity of MEG moiety versus toxic oxyanions to formulate a smart magnetic nanodevice for water remediation. Specifically, a novel approach was herein performed to cover SPION nanoparticles, testing their efficiency in removing As(V), Cr(VI), and B(III) from the water medium by batch experiment setup.

2. EXPERIMENTAL PART

2.1. Materials.
Meglumine (MEG), 4-vinyl-benzyl chloride, ammonium persulfate $[(NH_4)_2S_2O_8]$, sodium arsenate heptahydrate $(Na_2HAsO_4·7H_2O)$, potassium dichromate $(K_2Cr_2O_7)$, boric acid (H_3BO_3), poly-ethylene oxide (PEO), iron(III)chloride $(FeCl_3)$, and ammonium iron(II)sulfate

hexahydrate $[(NH_4)_2Fe(SO_4)_2(H_2O)_6]$ were purchased from Sigma-Aldrich and directly used. The solvents were used without further processes of purification. The monomer and the related polymer were previously synthesized and characterized as described below.

2.2. Synthesis of (4-Vinyl-benzyl)-meglumine (VbMEG).
The monomer was synthesized following the experimental methodology described by Mecca et al. MEG was suspended (1 g, 5 mmol) in 30 mL of CH_3OH and an equimolar amount of 4-vinyl-benzyl chloride (0.70 mL, 5 mmol) was added to the suspension in the presence of anhydrous Na_2CO_3.[29] The reaction mixture was stirred at room temperature, controlling the reaction progress by thin-layer chromatography. Then, the mixture was filtered and the methanol evaporated. The product was washed several times with cold $CHCl_3$ and dried under vacuum. The monomer was characterized by nuclear magnetic resonance (NMR) and infrared (IR) spectroscopy (see Figures S1 and S2).

2.3. Synthesis of Poly-(4-vinyl-benzyl)-meglumine (pVbMEG).
The polymerization of pVbMEG was carried out in a three-necked flask under a nitrogen atmosphere. The polymer was synthesized by dissolving 1 g of monomer in 10 mL of water. Ammonium persulfate was added as initiator (1% mol/mol). The stirred solution was heated up to 60 °C for 72 h. After cooling the mixture to room temperature, it was dropped in methanol.

Then, the product was filtered and washed with methanol up to three times. The pVbMEG was characterized by NMR, IR, and thermogravimetric analysis (TGA) (see Figures S3 and S5).

2.4. Synthesis of Functionalized Magnetite (Fe₃O₄) Nanoparticles.
2.4.1. Synthesis of Fe₃O₄ NPs. The nanostructured materials were prepared by co-precipitation methods. $FeCl_3$ and $(NH_4)_2Fe(SO_4)_2·6H_2O$ (Mohr's salt) have been chosen as nanoparticle precursors.

The reaction was carried out in a three-neck flask under a nitrogen atmosphere by dissolving the precursors in a Fe^{2+}/Fe^{3+} molar ratio of 1:2 in 100 mL of water. Sodium hydroxide was added as a base to promote the formation of mixed oxide. The solution was stirred for 30 min at 70 °C.

The obtained functionalized magnetic nanoparticles were filtered using a Buchner funnel and washed several times with distilled water to remove ionic species The synthesized nanomaterials was characterized by IR, TGA, X-ray diffraction (XRD), and vibrating-sample magnetometry (VSM).

2.4.2. Preparation of Fe₃O₄@MEG NPs. The functionalization of magnetite nanoparticles with meglumine was carried out following the same procedure described before but adding a freshly prepared 5% w/w aqueous solution of meglumine after adding the base. The mixture was stirred for 30 min at 70 °C. The obtained MNPs were filtered using a Buchner funnel and washed several times with distilled water to remove the ionic species.

2.4.3. Preparation of Fe₃O₄@ VbMEG NPs. A commercial PEO has been chosen to prepare freshly a 5% w/w aqueous solution and used to cover the MNPs as described above, obtaining the MNPs@PEO. After that, 1 g of as prepared MNPs was added in a round-bottom flask in the presence of 5% w/w aqueous solution of VbMEG. The exchange process between the two ligands was carried out under vigorous stirring at room temperature for 48 h. The product was filtered and washed several times.[49]
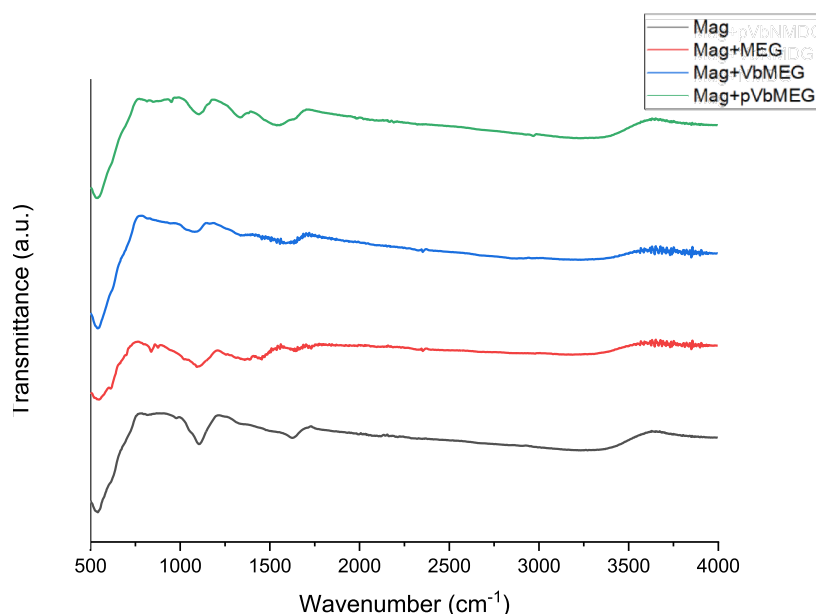
Figure 1. FT-IR spectra of the bare magnetite nanoparticles (black); MEG loaded on Fe_3O_4 (red); VbMEG loaded on Fe_3O_4 (blue); and poly-VbMEG loaded on Fe_3O_4 (green).

2.4.4. Preparation of Fe₃O₄@ pVbMEG NPs. The functionalization of magnetite nanoparticles with p-VbMEG was carried out adding a freshly prepared 5% w/w aqueous solution of polymeric ligands after the base addition during the as-reported magnetite nanoparticle preparation. The mixture was stirred for 30 min at 70 °C.

The obtained MNPs were filtered using a Buchner funnel and washed several times with distilled water to remove the ionic species.

2.5. Characterization Methods. The synthetized monomer and the polymer were accurately characterized. Their structures were confirmed by ^{1}H NMR spectroscopy by using a Varian "Mercury 400", operating at 400 MHz. TMS was used as an internal reference standard. The compounds were characterized by Fourier transform-infrared spectroscopy (FT-IR), the spectra were recorded through an ATR-IR Bruker Alpha I spectrometer. Thermal behavior was analyzed by TGA using a thermogravimetric apparatus (TA Instruments Q500) under a nitrogen atmosphere (flow rate 60 mL/min) and an air atmosphere at 10 °C/min heating rate, from 20 to 600 °C. TGA sensitivity is 0.1 μg with a weighting precision of ±0.01%. Powder XRD patterns were recorded on a PANalytical X'PertPRO X-ray diffractometer. A Cu radiation source (λ = 1.54 Å) was utilized, and diffraction patterns were recorded between 10 and 80 2θ over a scan time of 10 min. The synthesized nanostructured devices were characterized by scanning electric microscopy Thermo Phenom Prox desktop scanning electron microscopy (SEM) combined with a fully integrated energy-dispersive X-ray detector (Silicon Drift Detector) to evaluate size, morphology, and elemental composition of the samples. To further confirm the nanometric size of the prepared materials, dynamic light scattering (DLS) analysis were carried out by Malvern Zetasizer Nano ZS instrument, setting the experimental temperature at 25 °C and recording three sets of 25 scans to minimize the experimental error. Moreover, the poly dispersity-index (PDI) has been evaluated on a scale from 0 to 1, where the value of 0 represented the monodispersity condition. The magnetic

properties of nanostructured materials were investigated by means of hysteresis loops and first-order reversal curves by a Lakeshore 8604 vibrating sample magnetometer. Magnetic particles were placed into pharmaceutical gel caps #4 for their characterizations: the coercive force (B_c), the saturation remanent magnetization by mass (M_{rs}, or SIRM), and the saturation magnetization by mass (M_s) were measured at a maximum field of 1.0 T. Concentration-dependent hysteresis parameters were calculated subtracting the high field paramagnetic linear trend before dividing the magnetic moments for the net weight of the samples. The coercivity of remanence (B_{cr}) values was extrapolated from backfield re-magnetization curves up to −1.0 T after saturating at 1.0 T field. FORCs were measured in steps of 2.5 mT, with 100 ms averaging time and maximum applied field being 0.5 T using a Lakeshore 8604 VSM the Micromag operating software: FORC diagrams were processed, smoothed by Variforce, and drawn with the FORCINEL 3.05 Igor Pro routine.[50] The amount of metal anions in solution after the treatment with the synthesized nanomaterials was determined by an ICP−MS Nexion 300X (Perkin Elmer Inc. Waltham, Massachusetts, U.S.A.) using the kinetic energy discrimination (KED) mode for interference suppression.

2.6. Adsorption Test. The amount of metal anions in solution after the treatment with the synthesized nanomaterials was determined by an ICP−MS Nexion 300X (Perkin Elmer Inc. Waltham, Massachusetts, U.S.A.) using the KED for interference suppression. To evaluate the equilibrium retention capacity (Q_e) values and the metal ion removal percentage, a series of batch setup equilibrium tests were carried out.

In general, a specific amount of functionalized nanoparticles (5 mg) were dipped in 2.5 mL of each solution (pH = 6) containing metal anions at different initial concentrations, ranging from 500 to 16500 μg/L as metal concentration. The experiments were carried out at 25 °C under constant stirring (180 rpm) for 24 h. Several withdraws of 100 μL at different time intervals were fulfilled to investigate the kinetic behavior. By ICP−MS measurements the residual concentrations of
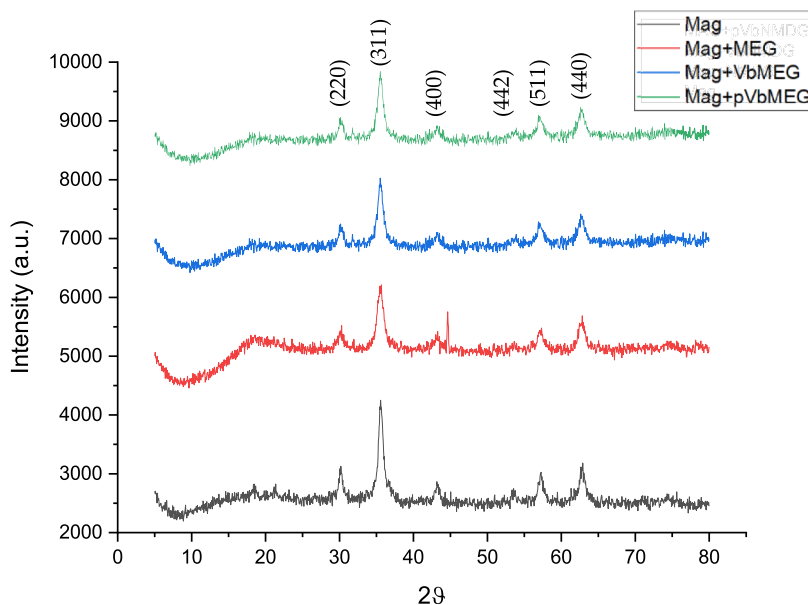
Figure 2. XRD pattern for the bare magnetite nanoparticles (black); MEG loaded on Fe_3O_4 (red); VbMEG loaded on Fe_3O_4(blue); and poly-VbMEG loaded on Fe_3O_4 (green).
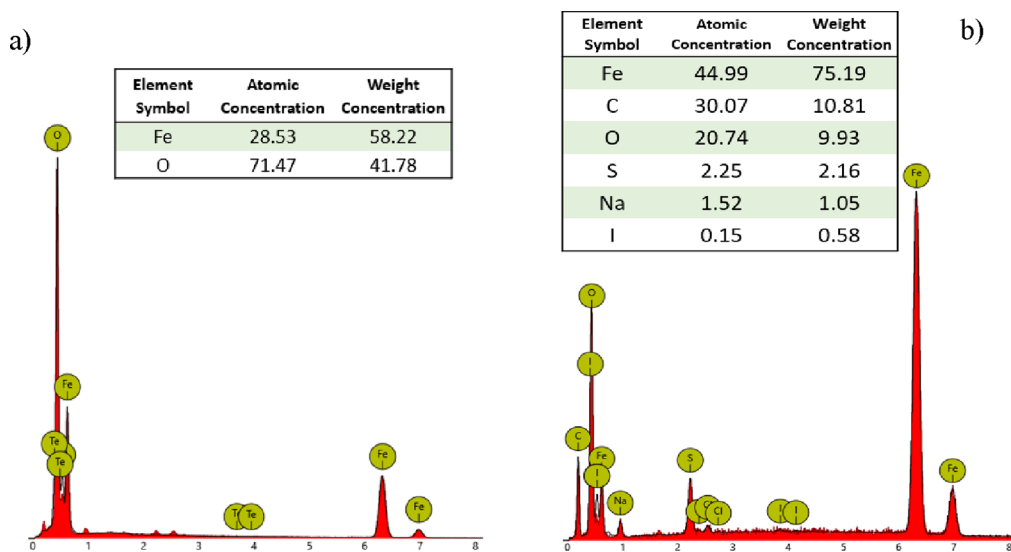

Element Symbol	Atomic Concentration	Weight Concentration
Fe	28.53	58.22
O	71.47	41.78

Element Symbol	Atomic Concentration	Weight Concentration
Fe	44.99	75.19
C	30.07	10.81
O	20.74	9.93
S	2.25	2.16
Na	1.52	1.05
I	0.15	0.58

Figure 3. EDX spectra related to bare Fe_3O_4 (a) and Fe_3O_4@ pVbMEG nanoparticles (b).

metal anions were evaluated. The kinetic phenomena were investigated by employing three different semiempirical adsorption kinetics: pseudo-first-order, pseudo-second-order, and intraparticle diffusion models.[51−53] The mathematical approach and the related equations applied are reported in the Supporting Information. In addition, several nonlinear isotherm models have been used in order to investigate the adsorption equilibrium of the Fe_3O_4−pVbMEG nanostructured material. In particular, Langmuir, Freundlich, Temkin, and Dubinin−Radushkevich isothermal adsorption models have been employed to understand the adsorbent−adsorbate interactions.[54−58] In the Supporting Information (see Figures S10−S12), the adsorption models and the physical parameters used to fit and correlate the observed adsorption process have been described.

3. RESULTS AND DISCUSSION

With the aim to cover SPIONs with polymeric ligands able to chelate metal ions, pVbMEG were synthetized by starting from

Table 1. DLS Diameters and PDI Values Related to the SPION Prepared

	Mag	Mag + MEG	Mag + VbMEG	Mag + PVbMEG
d_{DLS} (nm)	46	46	44	44
PDI	0.5	0.3	0.5	0.6

VbMEG. The reactions to produce the monomer have been already reported in the literature.[29] In light of this, the synthetic procedures to obtain it and related NMR, IR, and TGA characterizations are presented in the Supporting Information (Figures S1−S5).

Table 2. Hysteresis Parameters for the Bare Magnetite, MAG Loaded on Fe$_3$O$_4$, and Poly-VbMAG Loaded on Fe$_3$O$_4$: Values Are Mass Specific

	M_s (Am^2/kg)	M_{rs} (Am^2/kg)	B_c (mT)	B_{cr} (mT)
Mag	53.4	1.46	1.50	7.3
Mag + MEG	21.4	0.12	0.44	4.1
Mag + pVbMEG	38.3	0.36	0.25	4.1

The meglumine ligand and related based-monomer were used to functionalize the SPIONs by different approaches. Specifically, as described in the experimental section, the Fe$_3$O$_4$@meglumine NPs were prepared by a one-pot synthesis. Conversely, due to the high reactivity of the vinyl-benzyl monomer, whose can react at 70 °C forming the polymer into the aqueous solution, the one-pot methodology was not used, preferring a top-down strategy for the formulation of Fe$_3$O$_4$@VbMEG NPs. To this purpose (see the Experimental Part), a novel strategy consisting in the introduction of a preliminary coating agent based on PEO was tested. Subsequently, the ligand-exchange reaction was carried out in order to introduce the monomer VbMEG as a coating agent (Figure S8). In this view, the chemistry of the coated has been preserved, avoiding the polymerization reaction. As follows, a whole characterization of the as-prepared materials was described including their adsorption properties versus the selected metal ions targets.

3.1. Fe$_3$O$_4$ Nanostructured Material Characterization.

The FT-IR spectra of functionalized magnetite nanoparticles with meglumine, VbMEG, and pVbMEG are shown in Figure 1 and compared to the reference Fe$_3$O$_4$ NPs. A typical band at 580 cm^{-1} corresponding to the Fe−O bond stretching was observed. Moreover, the peak at 1100 cm^{-1} can be attributed to the stretching vibration of the Fe−OH formed during the synthetic route.[59]

The spectra of the Fe$_3$O$_4$@glucamine NPs, evidenced the appearance of new band at 1300 cm^{-1}, assigned to the C−N stretching of the related amine group. The signals emerged with a little intensity and are more evident in the system Fe$_3$O$_4$@pVbMEG. Lastly, a wide band at 1600 cm^{-1} corresponding to the aromatic moiety was observed in the samples synthesized by the monomer and polymer.

Despite the absence of defined signals, IR spectra confirmed the correct functionalization of the magnetite nanoparticles compared to the bare nanomaterial.

The successful coating of Fe$_3$O$_4$ nanostructured materials is further confirmed by XRD. The unit cell of the cubic spinel structure can be described with the follow structural formula of (Fe^{3+})$_A$[Fe^{2+}Fe^{3+}]$_B$O$_4$, where A and B represent if the ferrous and/or ferric ions are located in tetrahedral sites and octahedral sites, respectively.[60] Typically, magnetite can be easily oxidized in air at a temperature between 110 and 230 °C to form the maghemite (γ-Fe$_2$O$_3$) and when the temperature rises up above 250 °C, it can be further transformed to the hematite (α-Fe$_2$O$_3$). However, a typical magnetite inverse spinel structure can be observed in Figure 2 diffractograms, where it can be seen the main peaks at 2θ values of 30.1, 35.4, 43.1, 53.5, 57.9, and 63.0° corresponding to (220), (311), (400), (442), (511), and (440) Bragg reflection, respectively.[59] Characteristic diffraction peaks related to the other iron oxide structure are not revealed in the XRD pattern in Figure 2. Therefore, no other iron-based compounds are present into the as-prepared magnetite. Comparing the uncoated magnetite nanoparticles with the coated one, the XRD spectra exhibit similar diffraction peaks; this indicates that the coating agent does not have a significant effect on the crystal structure of the magnetite nanoparticles. In addition, the decrease of the nanoparticle size was observed due to the presence of the organic coating.

The crystalline size of nanostructured materials were calculated by the Debye−Scherrer equation: 12.4, 7.3, 9.2, and 9.7 nm are the sizes for the bare Fe$_3$O$_4$, MEG, VbMEG, and pVbMEG loaded on Fe$_3$O$_4$, respectively. The presence of coating agents plays an important role to reduce the magnetite nanoparticle size.

The thermograms related to the SPION-functionalized materials are complex results due to the presence of different degradation steps from 25 to 600 °C (Figure S6). The nanomaterials show a first stage around 200−220 °C related to the transformation from magnetite to maghemite. For the functionalized nanomaterials, in the second stage from 250 to 320 °C, weight loss occurred due to the thermal decomposition of the meglumine moiety. In this stage, the sample Fe$_3$O$_4$−VbMEG shows two distinct degradation temperatures,
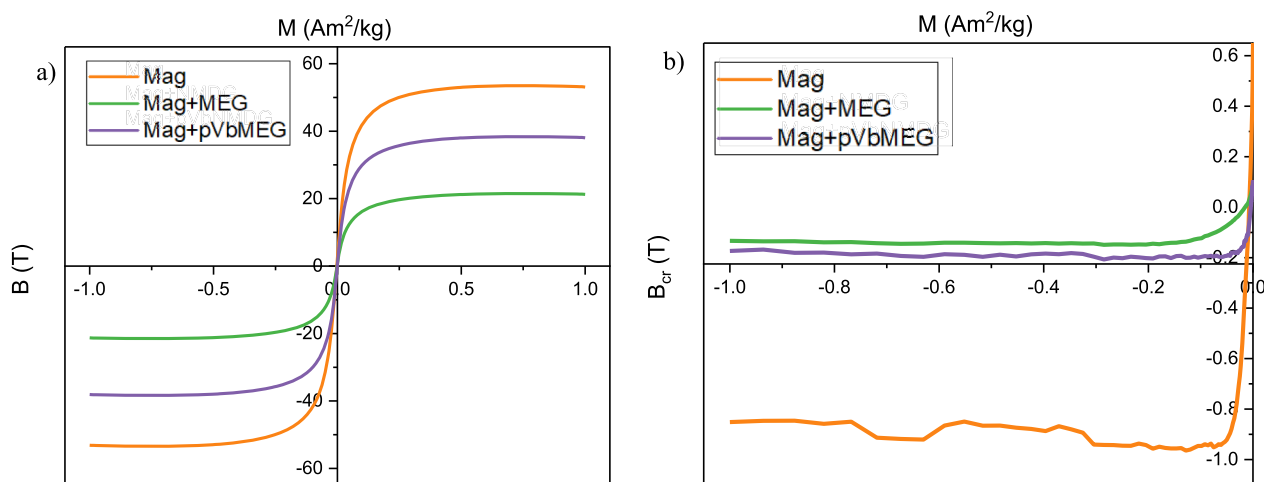

Figure 4. Hysteresis loops (a) and backfield applications after saturating at 1T magnetic field (b) for the bare magnetite, meglumine loaded on Fe$_3$O$_4$, and poly-VbMEG loaded on Fe$_3$O$_4$: the reported values are mass specific, hysteresis loops were corrected for the linear high field trend.
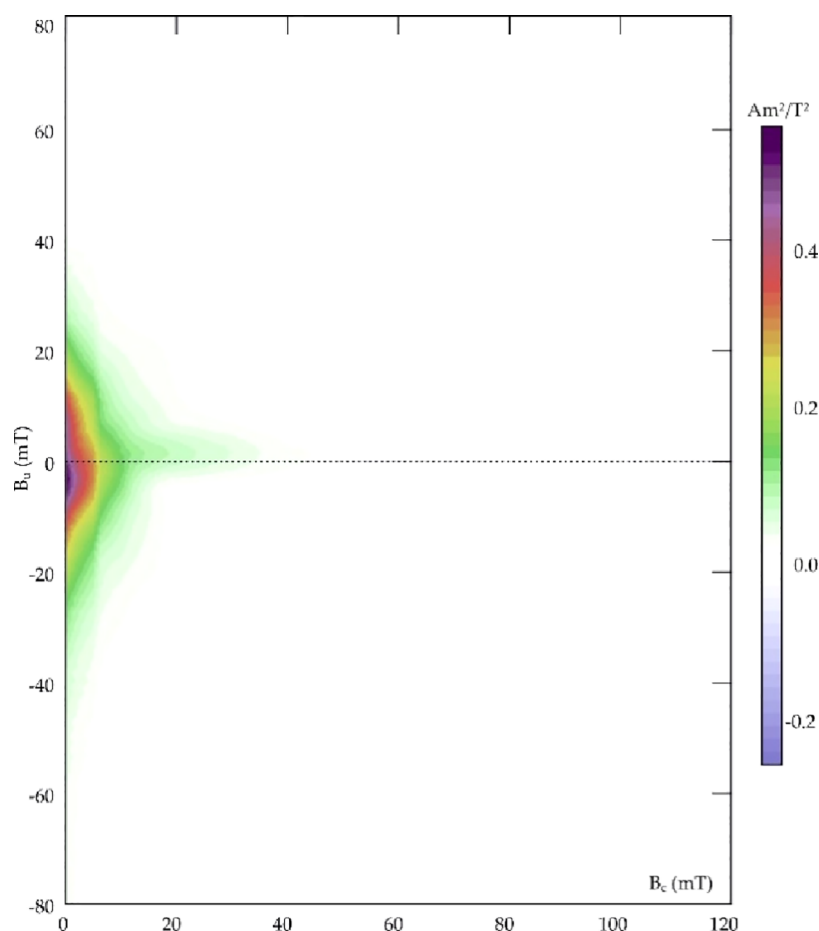
Figure 5. FORC diagram of pure magnetite sample, with asymmetric and low coercivity features typical for superparamagnetic particles; smoothing factor was 3 for the vertical and horizontal ridge and 5 for the background.

Table 3. Initial Concentration of Metal Ions (C_0), at the Equilibrium (C_e), Equilibrium Removal Capacity (Q_e), and Percentage of Metal Ions Removal after 24 h of Contact (R %)

As(V)				Cr(VI)				B(III)			
C_0 (μg L^{-1})	C_e (μg L^{-1})	Q_e (mg/g)	R %	C_0 (μg L^{-1})	C_e (μg L^{-1})	Q_e (mg/g)	R %	C_0 (μg L^{-1})	C_e (μg L^{-1})	Q_e (mg/g)	R %
500	1.7	0.58	99.7	500	1.1	0.25	99.8	500	77.4	0.21	84.5
1150	7.1	0.85	99.4	1150	2.5	0.57	99.8	1150	190.3	0.48	83.5
2500	162.9	1.30	93.5	2500	18.6	1.16	99.2	2500	354.4	1.1	85.8
8500	621.8	4.30	92.7	8500	358.8	4.07	95.8	8500	3022.5	2.7	64.4
16500	1398.6	8.25	91.5	16500	1488.1	7.50	90.9	16500	5928.2	5.3	64.1

whereas the nanostructured material obtained by the use of a polymer-like coating agent has a single step in which both degradative phenomena occurred. The third stage from 400 to 500 °C is presented only for the sample Fe$_3$O$_4$−pVbMEG, and this weight loss is attributed to the final decomposition of the polymeric structure by the breakage of its chain. TGA in an oxidative atmosphere was carried out in order to evaluate the functionalization degree of coated nanomaterials. The thermograms registered in the oxidative atmosphere show more degradative steps than the same samples analyzed under nitrogen. The degree of functionalization was calculated evaluating the amount of residue at the end of the analysis. The values obtained were 13, 11, and 10% of functionalization for meglumine loaded on Fe$_3$O$_4$; VbMEG loaded on Fe$_3$O$_4$; and pVbMEG loaded on Fe$_3$O$_4$, respectively (Figure S7).

Morphological data were obtained by using SEM (see the Experimental Part) up a magnification of 25k images (Figure S9) revealed a sub-micrometer size of the nanomaterials. In addition, by energy-dispersive X-ray (EDX) probe analysis, the correct functionalization of magnetite nanoparticles has been confirmed to the presence of elements such as carbon and oxygen related to the polymeric ligands in the sample Fe$_3$O$_4$@pVbMEG. From the images of bare magnetite nanoparticles can be observed the absence of carbon compared to the polymer-coated SPION system (Figure 3).

The DLS analysis were carried out to evaluate the nanometric size of prepared SPION's devices and to confirm the outcomes observed with the other characterization techniques. The samples Mag + MEG and Mag + VbMEG have been easily dispersed in water because the superficial functionalization has changed the solubility properties of the materials. On the other hand, the bare magnetite and Mag + pVbMEG were insoluble, and for this reason, the materials were dispersed in a meglumine solution for 24 h in order to
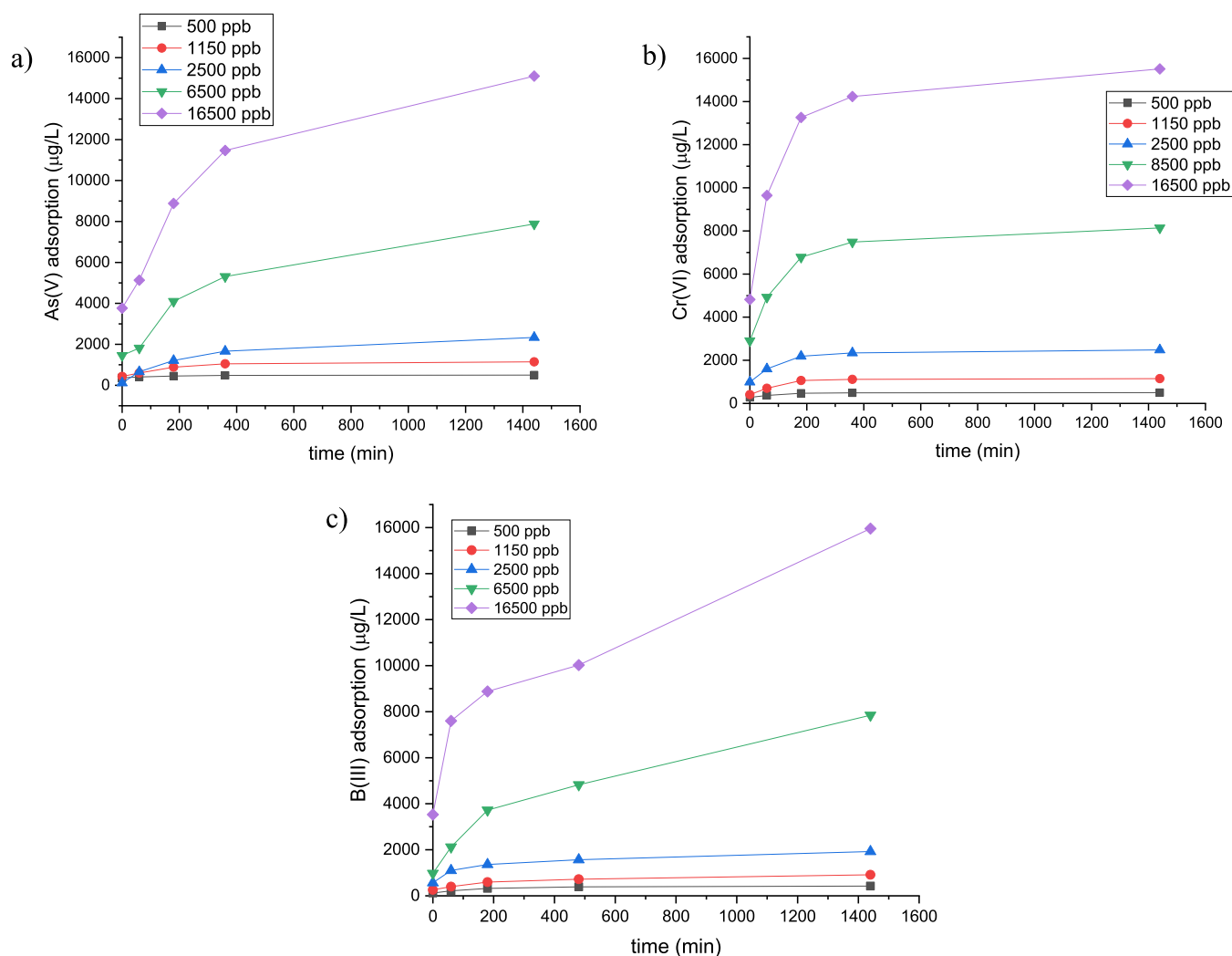
Figure 6. Amount of metal ion adsorbed as a function of time for (a) As(V), (b) Cr(VI), and (c) B(III) for different metal ion concentrations.

change the surface properties, improving the solubility. In particular, a post-synthesis approach has been employed to anchor the meglumine ligands on the bare nanooxides. Instead, the ligand-exchange reaction has been involved to change the polymeric ligands with the meglumine. Despite a partial aggregation in solution was observed due to the SPION magnetic behavior, the results obtained confirmed the nanosize of the materials prepared, nearby 45 nm was the hydrodynamic volume for all samples in agreement with the other analysis (Figure S10). In addition, slight poly-dispersity was observed with values around 0.5 of PDI. The average size and the related PDI values are reported in Table 1.

3.1.1. Magnetic Analysis. The magnetic properties of the synthesized materials were investigated. The magnetic hysteresis properties of Fe_3O_4, meglumine loaded on Fe_3O_4, and poly-VbMEG loaded on Fe_3O_4 have been measured to evaluate the contribution of different ligands on the magnetic power. In addition, FORC diagrams have been used for distinguishing between SP (superparamagnetic), SD (single domain), MD (multidomain), and PSD (pseudo single domain) behaviors according to the distributions of the interaction field (B_u) and the coercivity in samples. The hysteresis parameters and coercivity values are reported in Table 2. As revealed from Figure 4a, hysteresis loops were very narrow for all samples, well saturated before 1T, with almost

null B_c and, as highlighted in Figure 4b, very low values for both B_{cr} and saturation remanence field. This set of data is typical for magnetic mineralogizes dominated by ultrafine superparamagnetic particles (Figure 4a) that should theoretically have zero remanence and coercivity when measured at room temperature, adopting standard averaging times ≥ 100 ms. M_s was always lower than the bulk value for magnetite, that is, $90-92$ Am^2/kg. The decrease of M_s values with the reduction of particle size for magnetite can be explained in several ways, including spin disorder layer, which increases with the decrease in crystallite size, and dipolar interaction between magnetite nanoparticles. Moreover, the value of M_s can be influenced by the irregular morphology of magnetite particles due to surface anisotropy and incomplete crystallization after the reaction synthesis.[61,62] As observed from Mascolo and co-workers, the slope of the linear correlation between M_s and the particle size of magnetite decreased for the $6.5-8.0$ nm grain-size range, with respect to the $9-12$ nm interval.[63] In this sense, it is possible to confirm the trend observed by XRD spectra: according to the M_s values, the grain size of Mag + MEG is lower than that of Mag + pVbMEG and lower than that of bare magnetite nanoparticles. In Figure 5, the FORC diagram confirms the superparamagnetic ultrafine nature of magnetite particles. Indeed, the FORC diagrams of SP grains with relaxation times between 100 and 250 ms
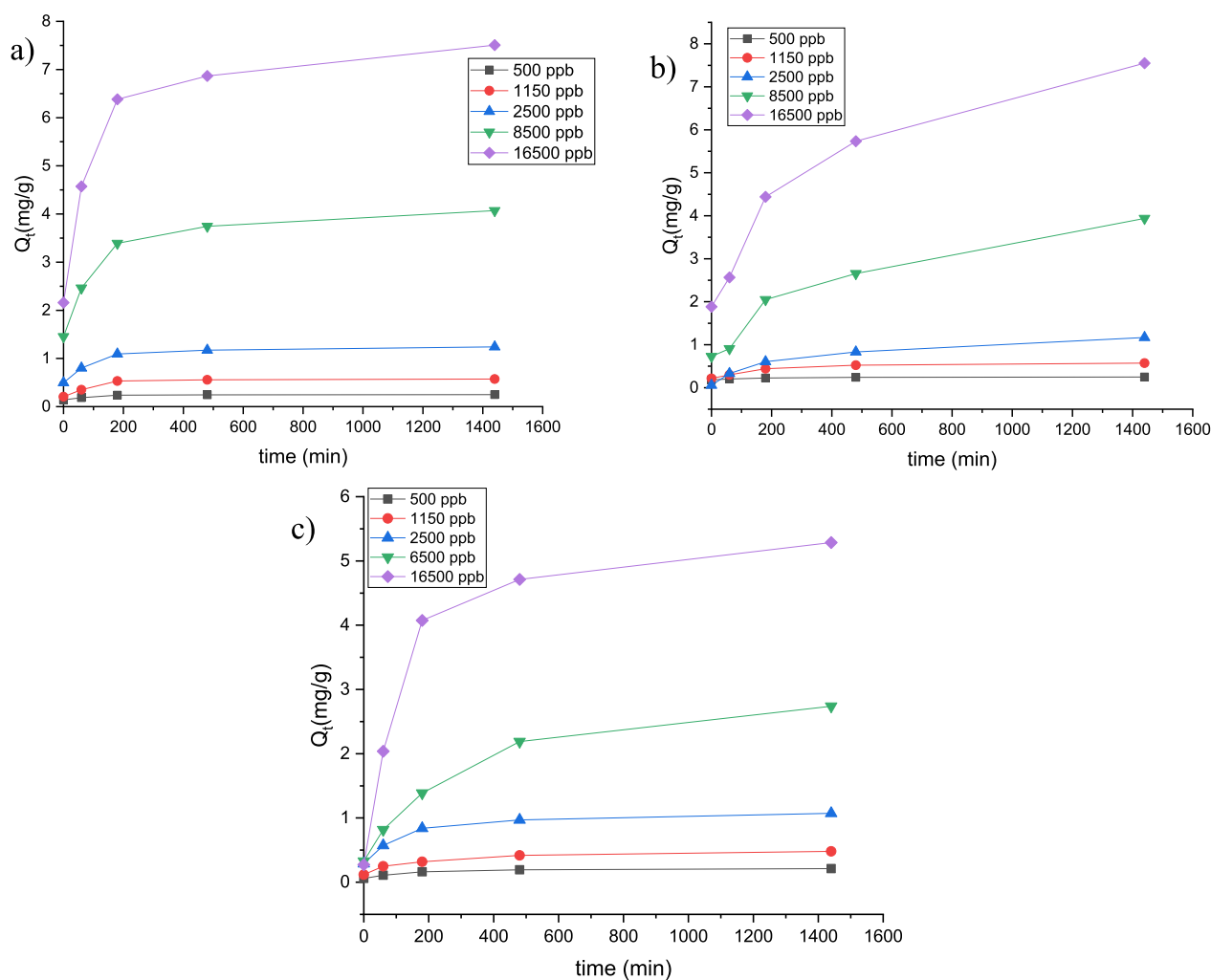
Figure 7. Kinetic profiles collected at room temperature of (a) As(V), (b) Cr(VI), and (c) B(III) adsorption calculated for different metal ion concentrations.

resemble those of MD grains, with distinguishable asymmetry and lower coercivity features.[64] The FORC diagrams reported for Mag + MEG and Mag + pVbMEG were similar but noisier, if compared to the pure magnetite, thus validating the grain size trend discussed above, and recalling that smaller superparamagnetic grains are unstable due to thermal agitation, so that the interaction field associated with such particles is not constant during the time it takes for a neighboring interacting magnetic moment to flip.[65] Independently from the nature of our samples, it is possible to conclude that the magnetic properties of the analyzed materials were dominated by ultrafine superparamagnetic features that, for magnetite, are carried by particles whose grain size is <35 nm.

3.2. Adsorption Study. In the first stage, to evaluate the adsorption ability of the intrinsically magnetic nanostructured materials versus the selected metal anions, preliminary tests were carried out taking in contact ~5 mg of each sample in metal ion solutions with a 500 ppb concentration of As(V). Only the Fe_3O_4 functionalized with pVbMEG was able to reduce the metal ion concentration. The other samples have showed high solubility in water due to the high hydro-solubility of the coating agent, as a consequence the materials taken in contact with the pollutant solution have been solubilized themself. Specifically, after 24 h of contact time, pVbMEG−Fe_3O_4 nanomaterials showed the best performance

in terms of metal ion uptake. Considering the results obtained, the effect of concentration as well as the kinetic and adsorption phenomena were widely investigated using pVbMEG−Fe_3O_4.

3.2.1. Concentration Effect. Batch equilibrium experiments were employed in order to investigate the concentration effect and quantify the adsorption capacity of pVbMEG loaded on magnetite nanoparticles as a function of As(V), Cr(VI), and B(III) concentration. For this reason, five different metal ions solutions were prepared with a concentration significantly higher than the permitted Word Health Organization (WHO) limits [10 μg/L, 50 μg/L, and 2.4 mg/L for As(V), Cr(VI), and B(III) respectively].[66] A defined amount of nanomaterials (5 mg) was used for each batch experiment. In Table 3 are reported the initial concentrations of the metal ion (C_0), the measured concentration at the equilibrium (C_e), the normalized equilibrium capacity (Q_e), and the calculated percentage of the metal ion retention after 24 h of contact time at room temperature and pH = 6. The batch experiments showed an efficient removal higher than 90% for As(V) and Cr(VI) ions for all the concentration analyzed. Instead, for the boron ions, a minor removal percentage was observed (Figure 6). Despite this, the B(III) equilibrium concentration values were lower than the WHO limit for the first concentrations tested (500, 1150, and 2500 ppb).
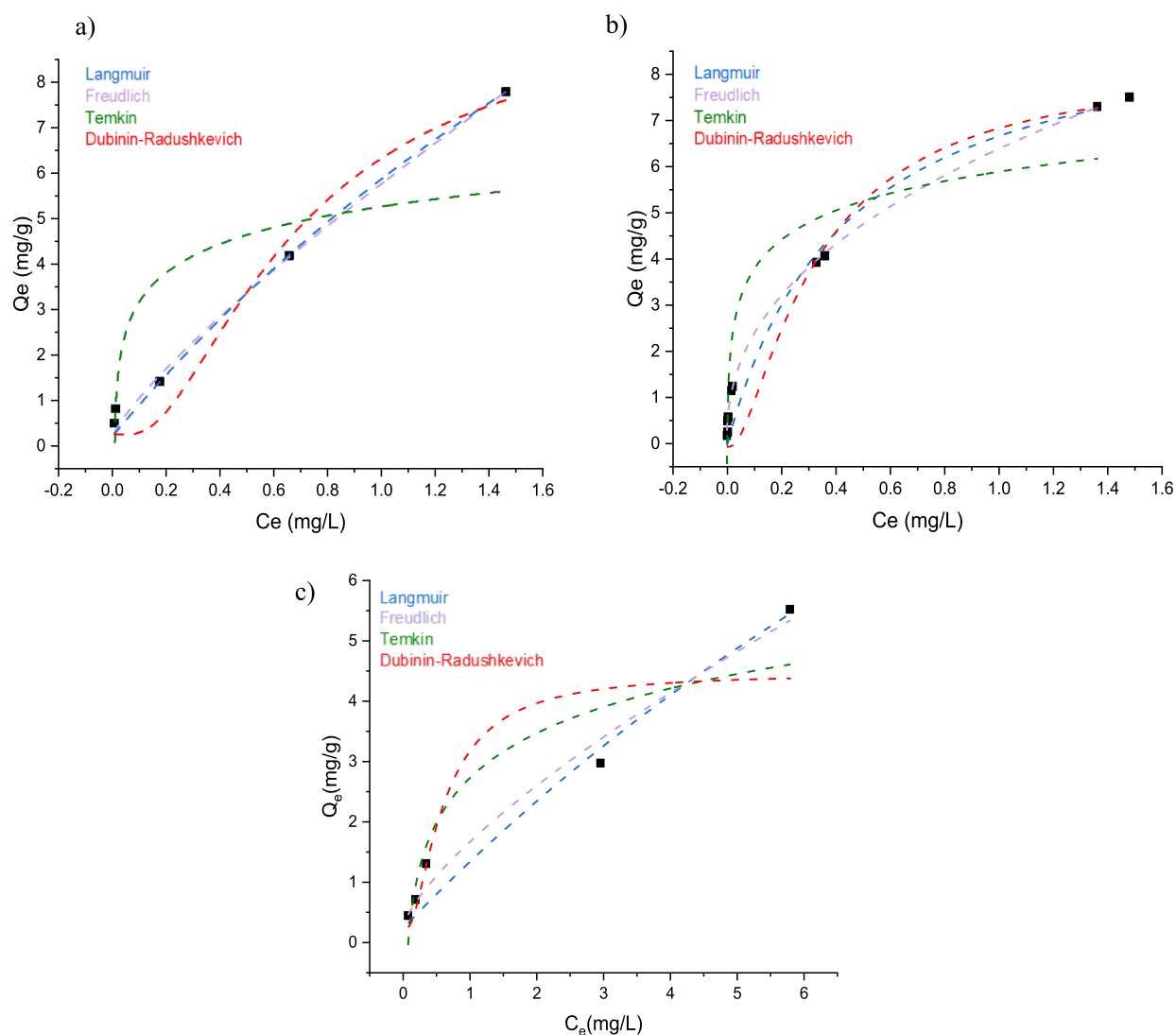
Table 4. Adsorption Kinetic Models of As(V), Cr(VI), and B(III) for Poly-VbMEG Loaded on Fe$_3$O$_4$ Fitted with the Pseudo-First-Order, the Pseudo-Second-Order, and the Intraparticle Diffusion Models

	As(V)					Cr(VI)					B(III)				
C_0 (μg/L)	500	1150	2500	8500	16500	500	1150	2500	8500	16500	500	1150	2500	8500	16500
Q_{exp} (mg/g)	0.3	0.6	1.2	3.9	7.6	0.3	0.6	1.2	4.1	7.5	0.2	0.5	1.1	2.7	5.3
Pseudo I-order															
K_1 (min^{-1})	4.6	4.1	2.4	2.0	2.4	6.2	6.3	4.8	4.1	4.1	4.4	3.0	3.1	3.5	4.4
R^2	0.99	0.98	0.95	0.94	0.97	0.88	0.88	0.89	0.92	0.86	0.91	0.99	0.94	0.98	0.97
Q_{et} (mg/g)	0.1	0.3	1.0	3.1	5.5	0.1	0.3	1.8	2.1	3.9	0.1	0.3	1.5	2.4	4.0
Pseudo II-order															
K_2 (min^{-1})	3.98	1.71	0.80	0.24	0.13	3.98	1.72	0.80	0.24	0.13	4.62	2.02	0.91	0.34	0.18
R^2	0.99	0.97	0.98	0.99	0.99	0.99	0.99	0.99	0.99	0.99	0.99	0.98	0.99	0.99	0.99
Q_{et} (mg/g)	0.3	0.6	1.2	4.2	7.9	0.3	0.6	1.2	4.1	7.6	0.2	0.5	1.1	2.9	5.5
Intraparticle Diffusion															
K_{Ip}	0.002	0.01	0.03	0.09	0.16	0.003	0.01	0.02	0.07	0.14	0.004	0.01	0.02	0.07	0.13
R_2	0.87	0.87	0.97	0.97	0.97	0.71	0.71	0.77	0.82	0.78	0.85	0.91	0.84	0.96	0.80

3.2.2. Adsorption Kinetic Profiles. Adsorption kinetic profiles were investigated in order to determine the adsorption equilibrium time. Different initial concentrations were employed for all experiments conducted, and similar adsorption trends can be observed (Figure 7): first, we have a significant increment for the first 3 h that level off at 6 h, reaching the equilibrium. In order to rationalize the kinetic behavior, three different models were used (Figures S11–S13). In particular, the better fitting for all metal ions analyzed in terms of R^2 values was obtained by applying the pseudo-second-order kinetic model. Moreover, to confirm the results observed, the theoretical adsorption capacity values (Q_{et}) and the experimental data were compared with each other (Table 4). Specifically, Q_{et} derived from the following equation reported in the Supporting Information (eq 1)

$$\frac{t}{Q_t} = \frac{1}{k_2 Q_e^2} + \frac{t}{Q_e} \tag{1}$$

showed a good match with the experimental values (Q_{exp}), conversely to those derived from eq 2 (in the Supporting Information) obtained by an interparticle diffusion model.

$$Q_t = k_i \sqrt{t} + C \tag{2}$$

By the trend extracted from the experimental data, a deviance from the linearity was observed applying the pseudo-first-order model probably derived to an intense adsorption during the initial phase of the process. Instead, the pseudo-second-order model data fitting allowed us to identify the surface adsorption of metal ions as a rate-limiting step in chemisorption. According to the literature, the pH represented a crucial parameter for the adsorption of metal anions. In particular, at the pH value employed (~6), the electrostatic attraction deriving from a protonated tertiary amine and the hydrogen bonds between the oxydrilic moieties of megluminic ligands control the adsorption process.[55,56,67] Moreover, the decrease of the kinetic constant values with the increase of initial metal ion concentrations suggested a surface saturation when high concentrations of metal ions were used, in agreement with the pseudo first and second kinetic models (see Table 4) (Figures S11–S13).

Instead, deviation from the linearity of the intraparticle diffusion was observed by kinetic profiles, and therefore, it is possible to not consider it as a rate-limiting step.

3.2.3. Adsorption Isothermal Models. To investigate the adsorption equilibrium, different isothermal models were employed. In Figure 8 and in Table 5 are reported the isothermal trends and the relative parameters for the adsorption of As(V), Cr(VI), and B(III). By analyzing the R^2 values, Langmuir and Freudlich models are the most corrected to describe the adsorption process of pVbMEG–Fe$_3$O$_4$ nanomaterials. Based on the Langmuir model, the maximum adsorption capacities (q_m) for As(V), Cr(VI), and B(III) are, respectively, 28.2, 12.3, and 23.7 (mg g^{-1}). These values are higher than the maximum capacity calculated by the Dubinin–Radushkevich model. Moreover, another parameter useful to analyze the adsorption efficiency is represented by the separation factor (R_L), and for the values derived from the Langmuir model being in the range of 0–1, the efficiency of the adsorption process is facilitated. Furthermore, the free energy of adsorption (E_{D-R}) obtained from the application of the Dublin–Radushkevich model described the nature of the metal ion/adsorbent interaction (e.g., physical, ion exchange,

Figure 8. Equilibrium adsorption isotherms collected at room temperature by plotting Q_e vs C_e experimental data for (a) As(V), (b), Cr(VI), and (c) B(III) for Fe$_2$O$_3$−pVbMEG.

Table 5. Isothermal Parameters Obtained by Applying Langmuir, Freundlich, Temkin, and Dubinin−Radushkevich Models for As(V), Cr(VI), and B(III), Testing Their Adsorption at Room Temperature
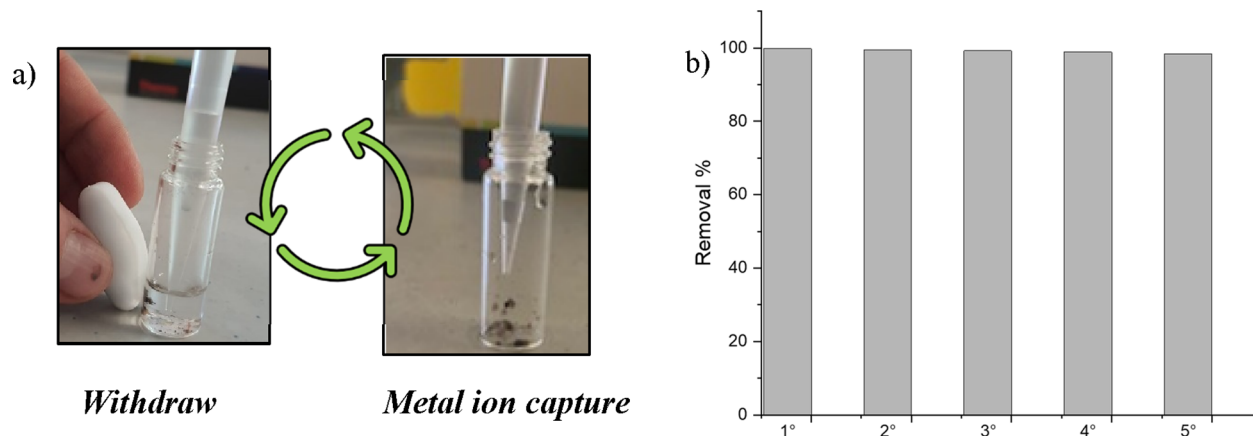
	Langmuir				Freundlich		
metal ion	q_m (mg/g)	K_L (L/mg)	R_L	R^2	K_F (mg/g)	n_F	R^2
As(V)	28.2	0.26	0.96−0.23	0.99	5.76		
	5.76	1.23	0.99				
Cr(VI)	12.3	1.09	0.64−0.052	0.97	6.34	2.38	0.99
B(III)	23.7	0.04	0.99−0.65	0.96	1.40	1.39	0.98

	Temkin			Dubinin−Radushkevich		
metal ion	B_T (kJ/mol)	K_T (L/mg)	R^2	q_m (mg/g)	$E_{D−R}$ (kJ/mol)	R^2
As(V)	0.89	0.29	0.70	9.47	1.9	0.96
Cr(VI)	0.93	0.60	0.87	8.31	2.80	0.93
B(III)	1.06	0.01	0.88	4.21	1.98	0.84

or chemisorption). As reported in the Supporting Information, when the $E_{D−R}$ is lower than 8 kJ/mol, the physical adsorption of metal anions was suggested. Regarding the type of interaction between the metal anions and the chelating sites, the driving force derives from the electrostatic interaction acted by the protonated amine group of meglumine. Moreover, also the hydroxyl groups play an active role in the

complexation mechanism. As reported by Reddy et al.,[74] the complexation of borate anions with the Meg moieties linked to a resin surface form stable mono- and bis-chelate complexes. These interactions were also evidenced for other ions tested in this paper.[29,75,76] Specifically, by using a combination of X-ray photoelectron spectroscopy, solid-state NMR, and FT-IR spectroscopy, Reddy et al. were able to identify and quantify

Table 6. Comparison of q_m Values of Different Adsorbent Materials Reported in the Most Recent Literature with the as-Synthesized pVbMEG−Fe$_3$O$_4$

year	adsorbent materials	As(V) q_m (mg g^{-1})	Cr(VI) q_m (mg g^{-1})	B(III) q_m (mg g^{-1})	pH	time of contact	reference
2021	pVbMEG−Fe$_3$O$_4$	28.2	12.3	23.7	6	24 h	this work
2021	waste foundry dust	12.6	2.42		3	24−48 h	68
2020	pVbNMG cryogel	76.3	130.9		6	24 h	29
2020	bare magnetite			6.9	6	10 h	69
2020	magnetic thiourea-formaldehyde resin	1.6	3.7		1−9	3 h	70
2019	NMDG@chitosan			19.9	7	10 h	71
2019	magnetite char	19.9			6	1 h	72
2010	IRA-743	14.7			6	3 d	73
2004	IRA-743		29.3		6	1 h	67

Figure 9. (a) Scheme of the purification process repeated up to five cycles. After 15 min of contact time, the Cr(VI) solution (1.15 mg/L) was removed as depicted. (b) ICP−MS of the withdrawn Cr(VI) solutions showed the removal of ∼99% up to five repeated cycles performed at room temperature.
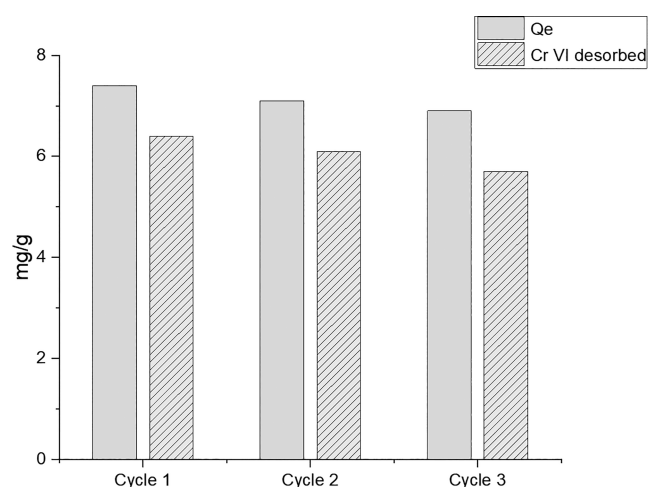
Figure 10. Regeneration experiment repeated up to three cycles at room temperature (C_0 = 17 mg/L, material = 5 mg).

boron adsorption sites as well as interactions between borate anions and hydroxyl groups of Meg moieties.

To evaluate the adsorption ability of different materials, the maximum adsorption capability parameter (q_m) can be used. In Table 5, the q_m values related to the synthesized nanostructured materials and analogue systems are reported and compared. In general, pVbMEG−Fe$_3$O$_4$ shows better performance in terms of q_m value if compared with the other materials reported in the literature and therefore presents a highly competitive ability versus As(V), Cr(VI), and B(III) sorption.

Commercially available IRA-743 showed a Cr(VI) maximum adsorption of 29.3 mg/g due to its cross-linked structure, and the material has a high amount of megluminic groups able to adsorb the metal ions. The same behavior was observed considering a polymeric cryogel formed on meglumine-functionalized units with adsorption capabilities of 76.3 mg/g and 130.9 mg/f for As(V) and Cr(VI), respectively. However, our nanostructured material is a combination of inorganic and organic parts, and the amount of MEG's moieties is necessarily lower in terms of total weight of adsorbent material rather than the corresponding amount present into a whole polymeric system. For this reason, the adsorption uptake observed is minor than the value reported for the organic resins. Moreover, a wide range of applicability in terms of kind of metal anions absorbed was noted for the materials synthesized in this work than the other reported in Table 6.

3.2.4. Reusability Test and Regeneration Cycles. The reusability of the synthesized nanomaterials has been evaluated by five successive absorption/separation cycles. The tests were carried out on the chromium solution in light of best adsorption data observed against this pollutant. The material was dipped in a dichromate solution containing 1150 ppb chromium VI and then separated by using a magnet to facilitate the removal of the solution after each subsequent reuse test. The treated solution was analyzed by ICP−MS to evaluate the remaining Cr(VI) after each purification step. Figure 9a,b shows the purification method adopted as well as the absorption efficiency of the material up to tested five cycles. As it is possible to appreciate from the histogram (Figure 9b), the removal efficiency remained almost

unchanged for all the tested cycles. To further exploit the potential of our material in terms of sustainability, together with the reusability, we also carried out the regeneration tests. Specifically, the material (5 mg) was immersed overnight in a solution of Cr(VI) (17000 ppb). Then, regeneration of nanoparticles was achieved by washing with 3 M NaOH solution, determining the Cr(VI) content in the eluted solution. After that, the sample was washed with water and reactivated by HCl 0.1 M. The regenerated material was retested with the same procedure for other three cycles showing good results (Figure 10).

4. CONCLUSIONS

A magnetic nanodevice based on magnetite nanoparticles coated by polymeric megluminic ligands able to absorb As(V), Cr(VI), and B(III) from the water matrix has been prepared. Functionalized nanostructured materials obtained by co-precipitation in water showed good uptake properties versus the metal anions analyzed even if present in low concentrations. Different spectroscopic and thermal analyses were carried out in order to investigate the composition of synthesized nanomaterials. Moreover, magnetic experiments were performed to confirm the magnetic grain size and domain state of the synthetized particles. Regarding the uptake process, $pVbMEG-Fe_3O_4$ sorption was well described by the Langmuir isotherm, the maximum adsorption capabilities (q_m) observed are 28.2, 12.3, and 23.7 mg/g for arsenic, chromium, and boron, respectively. In addition, the pseudo-second-order model best represents sorption kinetics; therefore, it is possible to identify the surface adsorption of ions as the rate-limiting step during the chemisorption. If compared with other similar materials present in the literature, $pVbMEG-Fe_3O_4$ exhibits good sequestering performances and a wide range of application in terms of kind of anions adsorbed. In addition, the synthesized nanomaterials have exhibited a good reusability after five cycles and an efficient strategy was developed to regenerate the materials by changing the pH value of the solution. The results obtained are the combination between the high superficial area derived from the magnetite nanostructure and the selectivity in the removal of the above metals due to the meglumine group that have allowed us to develop a novel magnetic device for the adsorption of metal anions from water..

■ ASSOCIATED CONTENT

Ⓢ Supporting Information

The Supporting Information is available free of charge at https://pubs.acs.org/doi/10.1021/acsomega.2c00558.

> ^{1}H NMR and IR spectra for the synthesized monomer and polymer; TGA for the synthesized polymer as well as the nanostructured materials prepared; SEM images of nanostructured materials; mathematic approach of adsorption; and kinetic models and As(V), Cr(VI), and B(III) adsorption kinetic profiles (PDF)

■ AUTHOR INFORMATION

Corresponding Author

Sandro Dattilo − *Istituto per i Polimeri, Compositi e Biomateriali, CNR-IPCB, 95126 Catania, Italy;* ⓞ orcid.org/0000-0002-3127-9580; Email: sandro.dattilo@cnr.it

Authors

Stefano Scurti − *Dipartimento di Chimica Industriale "Toso Montanari", University of Bologna, 40136 Bologna, Italy*
David Gintsburg − *Dipartimento di Chimica Industriale "Toso Montanari", University of Bologna, 40136 Bologna, Italy*
Luigi Vigliotti − *Istituto di Scienze Marine, ISMAR-CNR, 40129 Bologna, Italy*
Aldo Winkler − *Istituto Nazionale di Geofisica e Vulcanologia, 00143 Rome, Italy*
Sabrina Carola Carroccio − *Istituto per i Polimeri, Compositi e Biomateriali, CNR-IPCB, 95126 Catania, Italy;* ⓞ orcid.org/0000-0002-9645-0369
Daniele Caretti − *Dipartimento di Chimica Industriale "Toso Montanari", University of Bologna, 40136 Bologna, Italy*

Complete contact information is available at:
https://pubs.acs.org/10.1021/acsomega.2c00558

Notes

The authors declare no competing financial interest.

■ ACKNOWLEDGMENTS

■ REFERENCES

(1) Simeonidis, K.; Martinez-Boubeta, C.; Zamora-Pérez, P.; Rivera-Gil, P.; Kaprara, E.; Kokkinos, E.; Mitrakas, M. Implementing Nanoparticles for Competitive Drinking Water Purification. *Environ. Chem. Lett.* **2019**, *17*, 705−719.

(2) Schaider, L. A.; Senn, D. B.; Estes, E. R.; Brabander, D. J.; Shine, J. P. Sources and Fates of Heavy Metals in a Mining-Impacted Stream: Temporal Variability and the Role of Iron Oxides. *Sci. Total Environ.* **2014**, *490*, 456−466.

(3) Santhosh, C.; Malathi, A.; Dhaneshvar, E.; Bhatnagar, A.; Grace, A. N.; Madhavan, J. Iron Oxide Nanomaterials for Water Purification. In *Nanoscale Materials in Water Purification*; Elsevier, 2019; pp 431−446.

(4) Ali, I.; Peng, C.; Naz, I.; Amjed, M. A. Water Purification Using Magnetic Nanomaterials: An Overview. In *Magnetic Nanostructures*; Abd-Elsalam, K. A., Mohamed, M. A., Prasad, R., Eds.; Nanotechnology in the Life Sciences; Springer International Publishing: Cham, 2019; pp 161−179.

(5) Smedley, P. L.; Kinniburgh, D. G. A Review of the Source, Behaviour and Distribution of Arsenic in Natural Waters. *Appl. Geochem.* **2002**, *17*, 517−568.

(6) Demirbas, A. Heavy Metal Adsorption onto Agro-Based Waste Materials: A Review. *J. Hazard. Mater.* **2008**, *157*, 220−229.

(7) Mandal, B. Arsenic Round the World: A Review. *Talanta* **2002**, *58*, 201−235.

(8) Singh, A.; Sharma, R. K.; Agrawal, M.; Marshall, F. M. Health Risk Assessment of Heavy Metals via Dietary Intake of Foodstuffs from the Wastewater Irrigated Site of a Dry Tropical Area of India. *Food Chem. Toxicol.* **2010**, *48*, 611−619.

(9) Khan, S.; Cao, Q.; Zheng, Y. M.; Huang, Y. Z.; Zhu, Y. G. Health Risks of Heavy Metals in Contaminated Soils and Food Crops Irrigated with Wastewater in Beijing, China. *Environ. Pollut.* **2008**, *152*, 686−692.

(10) Fytianos, K.; Katsianis, G.; Triantafyllou, P.; Zachariadis, G. Accumulation of Heavy Metals in Vegetables Grown in an Industrial Area in Relation to Soil. *Bull. Environ. Contam. Toxicol.* **2001**, *67*, 423−430.

(11) Muchuweti, M.; Birkett, J. W.; Chinyanga, E.; Zvauya, R.; Scrimshaw, M. D.; Lester, J. N. Heavy Metal Content of Vegetables Irrigated with Mixtures of Wastewater and Sewage Sludge in Zimbabwe: Implications for Human Health. *Agric. Ecosyst. Environ.* 2006, 112, 41−48.

(12) Chowdhury, S.; Mazumder, M. A. J.; Al-Attas, O.; Husain, T. Heavy Metals in Drinking Water: Occurrences, Implications, and Future Needs in Developing Countries. *Sci. Total Environ.* 2016, 569−570, 476−488.

(13) Maurya, P. K.; Malik, D. S.; Yadav, K. K.; Kumar, A.; Kumar, S.; Kamyab, H. Bioaccumulation and Potential Sources of Heavy Metal Contamination in Fish Species in River Ganga Basin: Possible Human Health Risks Evaluation. *Toxicol. Rep.* 2019, 6, 472−481.

(14) Ali, H.; Khan, E.; Ilahi, I. Environmental Chemistry and Ecotoxicology of Hazardous Heavy Metals: Environmental Persistence, Toxicity, and Bioaccumulation. *J. Chem.* 2019, 2019, 1−14.

(15) Bolisetty, S.; Peydayesh, M.; Mezzenga, R. Sustainable Technologies for Water Purification from Heavy Metals: Review and Analysis. *Chem. Soc. Rev.* 2019, 48, 463−487.

(16) Baruah, G. L.; Nayak, A.; Belfort, G. Scale-up from Laboratory Microfiltration to a Ceramic Pilot Plant: Design and Performance. *J. Membr. Sci.* 2006, 274, 56−63.

(17) Matlock, M. M.; Howerton, B. S.; Atwood, D. A. Chemical Precipitation of Heavy Metals from Acid Mine Drainage. *Water Res.* 2002, 36, 4757−4764.

(18) Tay, P. K. R.; Nguyen, P. Q.; Joshi, N. S. A Synthetic Circuit for Mercury Bioremediation Using Self-Assembling Functional Amyloids. *ACS Synth. Biol.* 2017, 6, 1841−1850.

(19) Hernández Mata, K. M.; Monge Amaya, O.; Certucha Barragán, M. T.; Almendariz Tapia, F. J.; Acedo Félix, E. Metallic Biosorption Using Yeasts in Continuous Systems. *Int. J. Photoenergy* 2013, 2013, 1−4.

(20) Gupta, V. K.; Ali, I.; Saleh, T. A.; Nayak, A.; Agarwal, S. Chemical Treatment Technologies for Waste-Water Recycling—an Overview. *RSC Adv.* 2012, 2, 6380.

(21) Anjum, M.; Miandad, R.; Waqas, M.; Gehany, F.; Barakat, M. A. Remediation of Wastewater Using Various Nano-Materials. *Arab. J. Chem.* 2019, 12, 4897−4919.

(22) Fu, F.; Wang, Q. Removal of Heavy Metal Ions from Wastewaters: A Review. *J. Environ. Manage.* 2011, 92, 407−418.

(23) Wang, H.; Ji, X.; Ahmed, M.; Huang, F.; Sessler, J. L. Hydrogels for Anion Removal from Water. *J. Mater. Chem. A* 2019, 7, 1394−1403.

(24) Nicomel, N.; Leus, K.; Folens, K.; Van Der Voort, P.; Du Laing, G. Technologies for Arsenic Removal from Water: Current Status and Future Perspectives. *Int. J. Environ. Res. Publ. Health* 2015, 13, 62.

(25) Virolainen, S.; Heinonen, J.; Paatero, E. Selective Recovery of Germanium with N-Methylglucamine Functional Resin from Sulfate Solutions. *Sep. Purif. Technol.* 2013, 104, 193−199.

(26) Kabay, N.; Sarp, S.; Yuksel, M.; Arar, Ö.; Bryjak, M. Removal of Boron from Seawater by Selective Ion Exchange Resins. *React. Funct. Polym.* 2007, 67, 1643−1650.

(27) Urbano, B. F.; Rivas, B. L.; Martinez, F.; Alexandratos, S. D. Water-Insoluble Polymer−Clay Nanocomposite Ion Exchange Resin Based on N-Methyl-d-Glucamine Ligand Groups for Arsenic Removal. *React. Funct. Polym.* 2012, 72, 642−649.

(28) Caretti, D.; Binda, L.; Casis, N.; Estenoz, D. A. Novel Monomers with N -methyl- D - Glucamine Segments and Their Application in Structured Porous Materials for Arsenic Capture. *J. Appl. Polym. Sci.* 2022, 139, 51610.

(29) Mecca, T.; Ussia, M.; Caretti, D.; Cunsolo, F.; Dattilo, S.; Scurti, S.; Privitera, V.; Carroccio, S. C. N-Methyl-D-Glucamine Based Cryogels as Reusable Sponges to Enhance Heavy Metals Removal from Water. *Chem. Eng. J.* 2020, 399, 125753.

(30) Ting, T. M.; Nasef, M. M.; Hashim, K. Tuning N-Methyl- d -Glucamine Density in a New Radiation Grafted Poly(Vinyl Benzyl Chloride)/Nylon-6 Fibrous Boron-Selective Adsorbent Using the Response Surface Method. *RSC Adv.* 2015, 5, 37869−37880.

(31) Sayin, S.; Ozcan, F.; Yilmaz, M. Synthesis and Evaluation of Chromate and Arsenate Anions Extraction Ability of a N-Methylglucamine Derivative of Calix[4]Arene Immobilized onto Magnetic Nanoparticles. *J. Hazard. Mater.* 2010, 178, 312−319.

(32) Mahmoud Nasef, M.; Ting, T. M.; Abbasi, A.; Layeghimoghaddam, A.; Sara Alinezhad, S.; Hashim, K. Radiation Grafted Adsorbents for Newly Emerging Environmental Applications. *Radiat. Phys. Chem.* 2016, 118, 55−60.

(33) Ambashta, R. D.; Sillanpää, M. Water Purification Using Magnetic Assistance: A Review. *J. Hazard. Mater.* 2010, 180, 38−49.

(34) Gabrielli, C. Magnetic Water Treatment for Scale Prevention. *Water Res.* 2001, 35, 3249−3259.

(35) Hartikainen, T.; Nikkanen, J.-P.; Mikkonen, R. Magnetic Separation of Industrial Waste Waters as an Environmental Application of Superconductivity. *IEEE Trans. Appl. Supercond.* 2005, 15, 2336−2339.

(36) Zheng, X.; Xue, Z.; Wang, Y.; Zhu, G.; Lu, D.; Li, X. Modeling of Particle Capture in High Gradient Magnetic Separation: A Review. *Powder Technol.* 2019, 352, 159−169.

(37) Castelo-Grande, T.; Augusto, P. A.; Rico, J.; Marcos, J.; Iglesias, R.; Hernández, L.; Barbosa, D. Magnetic Water Treatment in a Wastewater Treatment Plant: Part I - Sorption and Magnetic Particles. *J. Environ. Manage.* 2021, 281, 111872.

(38) Chowdhury, S. R.; Yanful, E. K. Arsenic and Chromium Removal by Mixed Magnetite−Maghemite Nanoparticles and the Effect of Phosphate on Removal. *J. Environ. Manage.* 2010, 91, 2238−2247.

(39) Batool, S.; Akib, S.; Ahmad, M.; Balkhair, K. S.; Ashraf, M. A. Study of Modern Nano Enhanced Techniques for Removal of Dyes and Metals. *J. Nanomater.* 2014, 2014, 1−20.

(40) Tao, Q.; Bi, J.; Huang, X.; Wei, R.; Wang, T.; Zhou, Y.; Hao, H. Fabrication, Application, Optimization and Working Mechanism of Fe2O3 and Its Composites for Contaminants Elimination from Wastewater. *Chemosphere* 2021, 263, 127889.

(41) Baikousi, M.; Bourlinos, A. B.; Douvalis, A.; Bakas, T.; Anagnostopoulos, D. F.; Tuček, J.; Šafářová, K.; Zboril, R.; Karakassides, M. A. Synthesis and Characterization of γ-Fe$_2$O$_3$/Carbon Hybrids and Their Application in Removal of Hexavalent Chromium Ions from Aqueous Solutions. *Langmuir* 2012, 28, 3918−3930.

(42) Torasso, N.; Vergara-Rubio, A.; Rivas-Rojas, P.; Huck-Iriart, C.; Larrañaga, A.; Fernández-Cirelli, A.; Cerveny, S.; Goyanes, S. Enhancing Arsenic Adsorption via Excellent Dispersion of Iron Oxide Nanoparticles inside Poly(Vinyl Alcohol) Nanofibers. *J. Environ. Chem. Eng.* 2021, 9, 104664.

(43) Jazzar, A.; Alamri, H.; Malajati, Y.; Mahfouz, R.; Bouhrara, M.; Fihri, A. Recent Advances in the Synthesis and Applications of Magnetic Polymer Nanocomposites. *J. Ind. Eng. Chem.* 2021, 99, 1−18.

(44) Mehmood, A.; Khan, F. S. A.; Mubarak, N. M.; Tan, Y. H.; Karri, R. R.; Khalid, M.; Walvekar, R.; Abdullah, E. C.; Nizamuddin, S.; Mazari, S. A. Magnetic Nanocomposites for Sustainable Water Purification—a Comprehensive Review. *Environ. Sci. Pollut. Res.* 2021, 28, 19563−19588.

(45) Alam, E.; Feng, Q.; Yang, H.; Fan, J.; Mumtaz, S. Synthesis of Magnetic Core-Shell Amino Adsorbent by Using Uniform Design and Response Surface Analysis (RSM) and Its Application for the Removal of Cu2+, Zn2+, and Pb2+. *Environ. Sci. Pollut. Res.* 2021, 28, 36399−36414.

(46) Das, T. K.; Sakthivel, T. S.; Jeyaranjan, A.; Seal, S.; Bezbaruah, A. N. Ultra-High Arsenic Adsorption by Graphene Oxide Iron Nanohybrid: Removal Mechanisms and Potential Applications. *Chemosphere* 2020, 253, 126702.

(47) Yuan, P.; Fan, M.; Yang, D.; He, H.; Liu, D.; Yuan, A.; Zhu, J.; Chen, T. Montmorillonite-Supported Magnetite Nanoparticles for the Removal of Hexavalent Chromium [Cr(VI)] from Aqueous Solutions. *J. Hazard. Mater.* 2009, 166, 821−829.

(48) Ramos Guivar, J. A.; Sadrollahi, E.; Menzel, D.; Ramos Fernandes, E. G.; López, E. O.; Torres, M. M.; Arsuaga, J. M.;

Arencibia, A.; Litterst, F. J. Magnetic, Structural and Surface Properties of Functionalized Maghemite Nanoparticles for Copper and Lead Adsorption. *RSC Adv.* **2017**, *7*, 28763−28779.

(49) Hatakeyama, M.; Kishi, H.; Kita, Y.; Imai, K.; Nishio, K.; Karasawa, S.; Masaike, Y.; Sakamoto, S.; Sandhu, A.; Tanimoto, A.; Gomi, T.; Kohda, E.; Abe, M.; Handa, H. A Two-Step Ligand Exchange Reaction Generates Highly Water-Dispersed Magnetic Nanoparticles for Biomedical Applications. *J. Mater. Chem.* **2011**, *21*, 5959.

(50) Harrison, R. J.; Feinberg, J. M. FORCinel: An Improved Algorithm for Calculating First-Order Reversal Curve Distributions Using Locally Weighted Regression Smoothing: FORCINEL ALGORITHM. *Geochem., Geophys., Geosyst.* **2008**, *9*, 1−11, DOI: 10.1029/2008GC001987.

(51) Ho, Y. Review of Second-Order Models for Adsorption Systems. *J. Hazard. Mater.* **2006**, *136*, 681−689.

(52) *Adsorption Processes for Water Treatment and Purification*; Bonilla-Petriciolet, A., Mendoza-Castillo, D. I., Reynel-Ávila, H. E., Eds.; Springer International Publishing: Cham, 2017.

(53) Liu, C.-H.; Chuang, Y.-H.; Chen, T.-Y.; Tian, Y.; Li, H.; Wang, M.-K.; Zhang, W. Mechanism of Arsenic Adsorption on Magnetite Nanoparticles from Water: Thermodynamic and Spectroscopic Studies. *Environ. Sci. Technol.* **2015**, *49*, 7726−7734.

(54) Sutherland, C.; Venkobachar, C. A Diffusion-Chemisorption Kinetic Model for Simulating Biosorption Using Forest Macro-Fungus, Fomes Fasciatus. *Int. Res. J. Plant Sci.* **2010**, *1*, 107.

(55) Alberti, G.; Amendola, V.; Pesavento, M.; Biesuz, R. Beyond the Synthesis of Novel Solid Phases: Review on Modelling of Sorption Phenomena. *Coord. Chem. Rev.* **2012**, *256*, 28−45.

(56) Ramos Guivar, J. A.; Bustamante, D. A.; Gonzalez, J. C.; Sanches, E. A.; Morales, M. A.; Raez, J. M.; López-Muñoz, M.-J.; Arencibia, A. Adsorption of Arsenite and Arsenate on Binary and Ternary Magnetic Nanocomposites with High Iron Oxide Content. *Appl. Surf. Sci.* **2018**, *454*, 87−100.

(57) Bessaies, H.; Iftekhar, S.; Doshi, B.; Kheriji, J.; Ncibi, M. C.; Srivastava, V.; Sillanpää, M.; Hamrouni, B. Synthesis of Novel Adsorbent by Intercalation of Biopolymer in LDH for the Removal of Arsenic from Synthetic and Natural Water. *J. Environ. Sci.* **2020**, *91*, 246−261.

(58) Saadi, R.; Saadi, Z.; Fazaeli, R.; Fard, N. E. Monolayer and Multilayer Adsorption Isotherm Models for Sorption from Aqueous Media. *Korean J. Chem. Eng.* **2015**, *32*, 787−799.

(59) Petcharoen, K.; Sirivat, A. Synthesis and Characterization of Magnetite Nanoparticles via the Chemical Co-Precipitation Method. *Mater. Sci. Eng. B* **2012**, *177*, 421−427.

(60) Songvorawit, N.; Tuitemwong, K.; Tuitemwong, P. Single Step Synthesis of Amino-Functionalized Magnetic Nanoparticles with Polyol Technique at Low Temperature. *ISRN Nanotechnol.* **2011**, *2011*, 1−6.

(61) Daoush, W. M. Co-Precipitation and Magnetic Properties of Magnetite Nanoparticles for Potential Biomedical Applications. *J. Nanomed. Res.* **2017**, *5*, 00118.

(62) Bødker, F.; Mørup, S.; Linderoth, S. Surface Effects in Metallic Iron Nanoparticles. *Phys. Rev. Lett.* **1994**, *72*, 282−285.

(63) Mascolo, M.; Pei, Y.; Ring, T. Room Temperature Co-Precipitation Synthesis of Magnetite Nanoparticles in a Large PH Window with Different Bases. *Materials* **2013**, *6*, 5549−5567.

(64) Muxworthy, A. R.; Roberts, A. P. First-Order Reversal Curve (FORC) Diagrams. In *Encyclopedia of Geomagnetism and Paleomagnetism*; Gubbins, D., Herrero-Bervera, E., Eds.; Springer Netherlands: Dordrecht, 2007; pp 266−272.

(65) Muxworthy, A.; Heslop, D.; Williams, W. Influence of Magnetostatic Interactions on First-Order-Reversal-Curve (FORC) Diagrams: A Micromagnetic Approach: FORC Diagrams and Interactions. *Geophys. J. Int.* **2004**, *158*, 888−897.

(66) Organization, W. H. *Guidelines for Drinking-Water Quality*; World Health Organization, 1993.

(67) Gandhi, M. R.; Viswanathan, N.; Meenakshi, S. *Adsorption Mechanism of Hexavalent Chromium Removal Using Amberlite IRA 743 Resin*. 2010; Vol. *12*.

(68) Rha, S.; Jo, H. Y. Waste Foundry Dust (WFD) as a Reactive Material for Removing As(III) and Cr(VI) from Aqueous Solutions. *J. Hazard. Mater.* **2021**, *412*, 125290.

(69) Chen, T.; Wang, Q.; Lyu, J.; Bai, P.; Guo, X. Boron Removal and Reclamation by Magnetic Magnetite (Fe3O4) Nanoparticle: An Adsorption and Isotopic Separation Study. *Sep. Purif. Technol.* **2020**, *231*, 115930.

(70) Elwakeel, K. Z.; Shahat, A.; Al-Bogami, A. S.; Wijesiri, B.; Goonetilleke, A. The Synergistic Effect of Ultrasound Power and Magnetite Incorporation on the Sorption/Desorption Behavior of Cr(VI) and As(V) Oxoanions in an Aqueous System. *J. Colloid Interface Sci.* **2020**, *569*, 76−88.

(71) Wu, Q.; Liu, M.; Wang, X. A Novel Chitosan Based Adsorbent for Boron Separation. *Sep. Purif. Technol.* **2019**, *211*, 162−169.
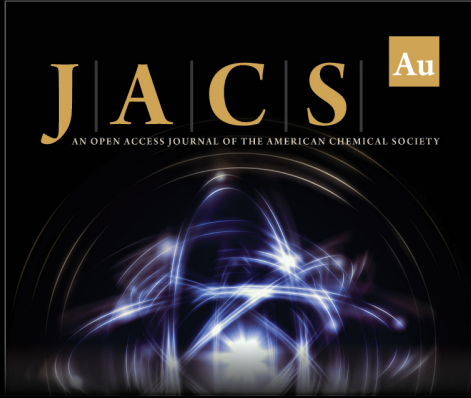
(72) Zubrik, A.; Matik, M.; Lovás, M.; Danková, Z.; Kaňuchová, M.; Hredzák, S.; Briančin, J.; Šepelák, V. Mechanochemically Synthesised Coal-Based Magnetic Carbon Composites for Removing As(V) and Cd(II) from Aqueous Solutions. *Nanomaterials* **2019**, *9*, 100.

(73) Dambies, L.; Salinaro, R.; Alexandratos, S. D. Immobilized *N*-Methyl-d-Glucamine as an Arsenate-Selective Resin. *Environ. Sci. Technol.* **2004**, *38*, 6139−6146.

(74) Reddy, G. N. M. Nanoscale Surface Compositions and Structures Influence Boron Adsorption Properties of Anion Exchange Resins. *Langmuir* **2019**, *35*, 15661−15673.

(75) Bryjak, M., Kabay, N., Rivas, B. L., Bundschuh, J., Eds. *Innovative Materials and Methods for Water Treatment: Solutions for Arsenic and Chromium Removal*; CRC Press, 2016; Vol. *2*.

(76) Kamcev, J.; Taylor, M. K.; Shin, D. M.; Jarenwattananon, N. N.; Colwell, K. A.; Long, J. R. Functionalized Porous Aromatic Frameworks as High-Performance Adsorbents for the Rapid Removal of Boric Acid from Water. *Adv. Mater.* **2019**, *31*, 1808027.